Novel Concepts for Integrating the Electric Drive and Auxiliary DC–DC Converter for Hybrid Vehicles

Hanna Plesko, *Student Member, IEEE*, Jürgen Biela, *Member, IEEE*, Jorma Luomi, *Member, IEEE*, and Johann W. Kolar, *Senior Member, IEEE*

***Abstract*—Cost, volume, and weight are three major driving forces in the automotive area. This is also true for hybrid electric vehicles, which are attracting more and more attention due to increasing fuel costs and air pollution. In hybrid vehicles, the energy distribution system causes a significant share of the volume and the costs. One part of this system is the dc–dc converter that transfers power between the low- and high-voltage buses. In order to reduce the costs and the volume of this converter, this paper presents a new concept for integrating the dc–dc converter functionality into the traction drive system. By using the inverter and the machine to implement a primary bridge leg of an isolated full-bridge dc–dc converter, the total system costs and weight can be reduced. This concept is verified by simulations and experimental results for a scaled prototype. An analytical model of the system has been developed and agrees very well with the measurements. By scaling this model to the power levels typical for hybrid vehicles, it is expected that the efficiency for the dc–dc converter will be greater than 85% for a conventional modulation scheme and above 91% for an optimized switching scheme.**

***Index Terms*—Electric vehicle motor drives, novel power converter topologies for vehicle drives.**

I. Introduction

GROWING fuel cost is just one factor that is driving the development of hybrid electric vehicles [1]. Today, there are several car manufacturers producing hybrid vehicles and the research activities in this area are growing. Fig. 1 shows the common voltage levels and interconnections for the electric power system of a hybrid vehicle.

Conventional mild- and full-hybrid electric vehicles usually have two different voltage levels. The 14-V dc bus is often supplied by a 12 V battery. Traditional loads, such as fans and lighting systems, are connected to this low-voltage bus. In addition, there is a high-voltage 200–600-V dc bus, which provides the necessary power for the propulsion system, and is connected to the low-voltage bus via a bidirectional dc–dc converter. This converter needs to be galvanically isolated for safety reasons. The supply voltages of the electric machine are produced by a dc–ac converter connected to the high-voltage bus.

Manuscript received January 25, 2008; revised April 9, 2008. First published November 25, 2008; current version published December 9, 2008. This paper was presented in part at the Applied Power Electronics Conference 2007 in Los Angeles, CA, February 2007. Recommended for publication by Associate Editor J. Ojo.

H. Plesko, J. Biela, and J. W. Kolar are with the Power Electronic Systems Laboratory, Swiss Federal Institute of Technology Zurich ETH-Zentrum, Zurich 8092, Switzerland (e-mail: plesko@lem.ee.ethz.ch; biela@lem.ee.ethz.ch; kolar@lem.ee.ethz.ch).

J. Luomi is with Helsinki University of Technology, Espoo FIN-02015, Finland (e-mail: jorma.luomi@tkk.fi).

Digital Object Identifier 10.1109/TPEL.2008.2005384

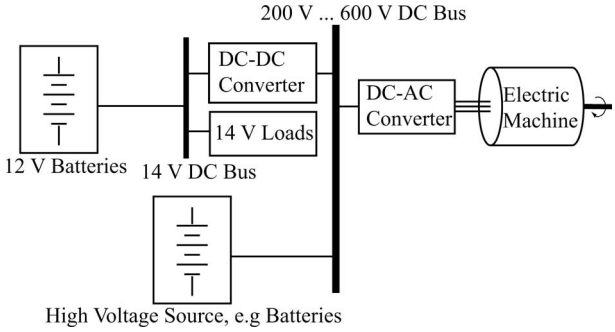

Fig. 1. One possibility of a conventional electrical power distribution system architecture for hybrid electric vehicles.

In recent years, the growing number of additional electrical loads forced the car industry to consider the introduction of an additional 42-V dc bus, supplied via a 36 V battery [2], in addition to the 200–600-V voltage source. In a first step, the conventional 14 V level is also installed, since most of the traditional loads are designed for 14 V operation. In the future, the 14 V bus would be omitted for cost savings. However, the functionality of the converter proposed in this paper is independent of these changes. Another possibility is to omit the 200–600 V high-voltage level and to supply the propulsion system with 42 V, as proposed by Toyota for their mild hybrid system (THSM). As the advantages of the high-voltage solution outweigh those of the 42 V variant, as shown in [3], it is assumed in the following that the propulsion system is fed via a 200–600 V high-voltage bus.

In order to reduce the costs of the electric system and increase the power density, the dc–dc converter linking the low- and high-voltage buses could be functionally integrated into the inverter and/or electric machine. For example, in [4], a possible integration of the dc–dc converter in the inverter system is presented, but it is applicable only for split-phase motors. Another integration possibility is described in [5], which is, however, not galvanically isolated. In [5], galvanic isolation is not required, since the high-voltage bus is omitted and the electrical machine is fed from 42 V. There, the zero-sequence voltage at the machine's star point is used to bidirectionally transfer power between the high- and low-voltage dc buses. The output voltage is controlled by choosing an appropriate switching scheme (see Fig. 2). The inverter operates as a buck–boost converter and the machine's zero-sequence inductance serves as the buck–boost inductor. Similar concepts without galvanic isolation have been presented in [6]–[8] and [9].

As mentioned earlier, it would be desirable to feed the propulsion system from the high-voltage bus. The concept proposed

0885-8993/$25.00 © 2008 IEEE

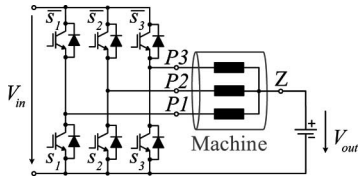

Fig. 2. Concept of integration without isolation.

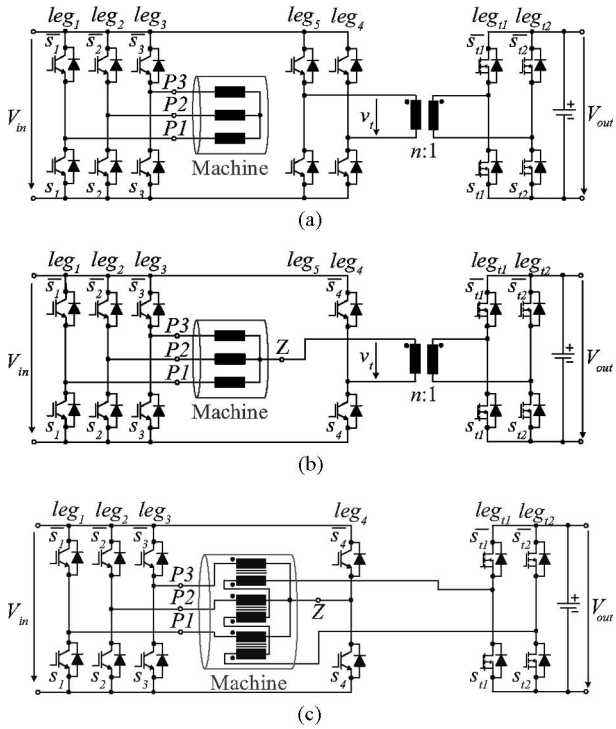

Fig. 3. Multifunctional converter systems (MFCS). (a) Separated dc–dc converter and inverter. (b) Proposed integrated dc–dc converter: MFCS-I. (c) Proposed integrated dc-dc converter: MFCS-II.

in [5] cannot be used since the high-voltage to low-voltage converter needs to have galvanic isolation for safety reasons. In addition, the output voltage $V_{\rm out}$ of the dc–dc converter cannot be controlled in every operating region of the drive system. If the inverter operates, for example, in the six-step mode, the switching state of the inverter is totally determined. There is no DOF for controlling the output voltage. To overcome these problems, an integrated high-voltage to low-voltage dc–dc converter with galvanic isolation is proposed in this paper. Depending on the actual distribution system, this converter can be used to convert 200–600 V to 14 V or 42 V bidirectionally.

The starting point for the following consideration is a conventional full-bridge converter feeding a high-frequency transformer [see Fig. 3(a)], whose high-frequency output is rectified to the output voltage $V_{\rm out}$. The secondary-side rectifier could be a conventional full-bridge configuration, or a diode rectifier, if only the unipolar power transfer is required.

In a first step, the fifth leg [i.e., leg_5 in Fig. 3(a)] of the conventional system is replaced by the zero-sequence voltage. There, the transformer is connected between the star point and the midpoint of the primary-side leg four [see Fig. 3(b)]. This concept is referred to as the multifunctional converter system I (MFCS-I) [10] in the following.

In a second step, the iron core of the motor could be used for integrating the transformer, as shown in Fig. 3(c). Compared to the conventional machine, there is an additional secondary winding for each phase. As these secondary windings are connected in series, the total voltage appearing on the secondary side is proportional to the zero-sequence voltage of the machine in the no-load case. Section III gives a more detailed report of this concept, referred to as the multifunctional converter system II (MFCS-II) [11]. Other possibilities of using the iron core of the motor or the input inverter for integrating the transformer are presented in [12] and [13], but the concept proposed here saves space compared to [12] and [13] because it does not need a three-phase rectifier.

In this paper, the basic function of the first variant, the MFCS-I, is explained, and it is shown by simulations and experimental results that this concept works well. In Section II-A, the basic operating principle of the MFCS-I is explained by studying the zero-sequence voltage and introducing an equivalent circuit for the dc–dc converter, followed by a more detailed analysis in Section II-B that focuses on the control. The simulation results presented in Section II-C validate the analytical model. Section II-D presents a detailed analysis of the zero-sequence impedance and a motor model. The theoretical results are verified experimentally using a 3 kW prototype in Section II-E, and the efficiency is analyzed in Section II-F. In Section III, the second variant, the MFCS-II, is briefly discussed. Finally, a conclusion is given in Section IV.

II. MFCS-I

In the MFCS-I, the transformer is connected to the star point and the output of the fourth leg [i.e., leg_4, in Fig. 3(b)], thus eliminating one leg of the full-bridge converter compared to the conventional system.

A. Basic Principle of Operation—MFCS-I

Both concepts, MFCS-I and MFCS-II, are based on the utilization of the zero-sequence voltage, whose definition and calculation are summarized before the details of the concepts are explained. The zero-sequence voltage of a three-phase system is defined as

$$v_z = \frac{1}{3}(v_{P1} + v_{P2} + v_{P3}) \tag{1}$$

where v_{P1}, v_{P2}, and v_{P3} are the phase-to-neutral voltages applied to the machine. Depending on the switching state of the inverter, the zero-sequence voltage related to the negative bus bar can be calculated as

$$v_z = \frac{V_{\rm in}}{3}(\overline{s_1} + \overline{s_2} + \overline{s_3}) \tag{2}$$

where $\overline{s_\nu} = 1$ if $\overline{s_\nu}$ is closed and s_ν is open, else $\overline{s_\nu} = 0$, and $V_{\rm in}$ is the input voltage (see Fig. 3).

Fig. 4(a) shows the zero-sequence voltage for conventional space vector modulation with an input voltage $V_{\rm in} = 50$ V, a switching frequency $f_{\rm sw} = 10$ kHz, an electrical angular motor

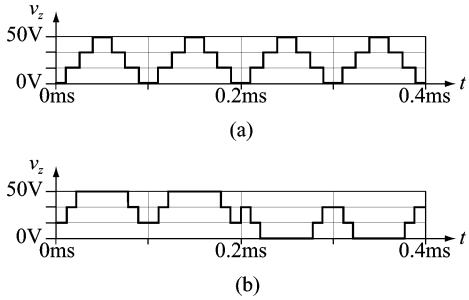

Fig. 4. Zero-sequence voltage v_z for $M = 0.5$, $f = 25$ Hz, $f_{\rm sw} = 10$ kHz, and $V_{\rm in} = 50$ V for (a) conventional and (b) flat top modulation.

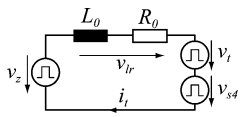

Fig. 5. Equivalent circuit for the dc–dc converter.

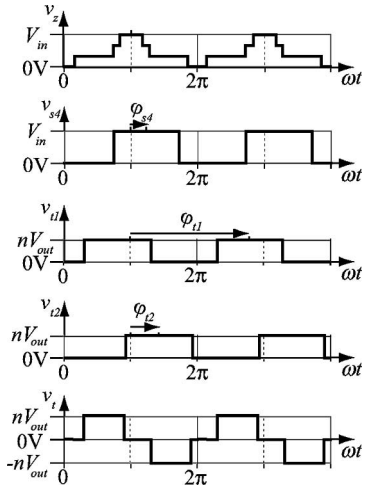

Fig. 6. Converter waveforms: zero-sequence voltage v_z, voltage v_{s4} across s_4, voltage v_{t1} across s_{t1}, voltage v_{t2} across s_{t2}, and transformer voltage v_t.

frequency $f = 25$ Hz, and a modulation index $M = 0.5$. The same signal is shown in Fig. 4(b) for flat top modulation, where the phase with the highest absolute current value is clamped to the positive bus if this current is positive; otherwise, it is clamped to the negative bus.

If the inverter is operated in a six-step mode, the zero-sequence voltage remains constant for a sixth of period of the motor frequency. Without the leg, leg_4 [see Fig. 3(b)], the six-step operation would lead to a transformer voltage with a very low frequency. In order to keep the transformer's volume small and to prevent the transformer from saturating, proper pulsing of s_4 and $\overline{s_4}$ is required.

For the dc–dc converter, the only important part of the inverter–machine subsystem is the zero-sequence impedance and the zero-sequence voltage v_z, which can be calculated by (2). Thus, the integrated dc–dc converter can be modeled, as shown in Fig. 5. The time-dependent voltage source v_z represents the zero-sequence voltage and v_{s4} describes the voltage across s_{s4} [see Fig. 3(b)]. These two voltage sources are connected to an LR circuit, modeling the machine's zero-sequence impedance. Voltage v_t represents the transformer voltage [see Fig. 3(b)].

It has to be mentioned that v_z, as defined in (2), can only be measured if no zero-sequence current flows; otherwise, it is a theoretical quantity since there is a voltage drop v_{lr} across L_0 and R_0. The voltage measured between the star point and the negative bus is equal to $v_z - v_{lr}$.

This system is similar to a full-bridge rectifier system, but as the voltage v_z applied to the system is neither average free (related to the switching frequency) nor free from even harmonics, a conventional modulation scheme cannot be adopted.

In the actual implementation, an active rectifier is used to guarantee that the voltage-time product across the transformer remains below a predetermined level. The described dc–dc converter is similar to a dual active bridge [14], [15]. A unidirectional implementation with a diode rectifier would be another possibility, but in order to limit the voltage-time product across the transformer, a special control approach has to be implemented.

B. Control of MFCS-I

It is assumed, without loss of generality, that the motor is driven with space vector modulation and the required switch dead time is neglected.

It is clear that the average zero-sequence voltage over a switching frequency period is not always $\frac{V_{\rm in}}{2}$ related to the negative bus bar but may depend on the motor's electric angle ωt. The average can be calculated as

$$v_{z_{\rm avg}} = \frac{U_1}{3}\left(\delta_{s1} + \delta_{s2} + \delta_{s3}\right) \tag{3}$$

where $\delta_{s\nu}$ is the relative OFF time of s_ν, depending on the motor's angle and the actual modulation index. To avoid saturation of the transformer, it is necessary that the applied voltage does not show a local average value. This restriction means for the fourth leg, which compensates for the average value, that the relative OFF time δ_{s4} of s_{s4} is determined by the zero-sequence voltage as

$$\delta_{s4} = \frac{1}{3}(\delta_{s1} + \delta_{s2} + \delta_{s3}). \tag{4}$$

The only DOF is the relative phase shift between the zero-sequence voltage v_z and the fourth-leg voltage v_{s4}, represented by the angle φ_{s4} (see Fig. 6).

Further, the voltage on the secondary side of the transformer has to be average free, which means that the relative ON times of s_{t1} and s_{t2} are 50% in steady-state operation. The angular shifts of the switch voltages v_{t1} and v_{t2} are denoted by φ_{t1} and φ_{t2}, respectively.

The Fourier series of the three voltages v_z, v_{s4}, and v_t for the switching frequency $f_{\rm sw}$ can be described as

$$v_z = a_{z(0)} + \sum_{k=1}^{\infty} a_{z(k)} \cos(k\omega_{\rm sw} t)$$

$$v_{s4} = a_{s4(0)} + \sum_{k=1}^{\infty} a_{s4(k)} \cos(k\omega_{\rm sw} t - k\varphi_{s4})$$

$$v_t = \sum_{k=1}^{\infty} a_{t(k)} [\cos(k\omega_{\rm sw} t - k\varphi_{t1}) - \cos(k\omega_{\rm sw} t - k\varphi_{t2})] \quad (5)$$

where $\omega_{\rm sw} = 2\pi f_{\rm sw}$ and

$$a_{z(k)} = \begin{cases} -\dfrac{2V_{\rm in}}{3k\pi}[\sin(k\pi\delta_a) + \sin(k\pi\delta_b) + \sin(k\pi\delta_c)], & \text{for } k \text{ odd} \\ \dfrac{2V_{in}}{3k\pi}[\sin(k\pi\delta_a) + \sin(k\pi\delta_b) + \sin(k\pi\delta_c)], & \text{for } k \text{ even.} \end{cases}$$

$$a_{s4(k)} = \begin{cases} -\dfrac{2V_{\rm in}}{k\pi}\sin(k\pi\delta_{s4}), & \text{for } k \text{ odd} \\ \dfrac{2V_{\rm in}}{k\pi}\sin(k\pi\delta_{s4}), & \text{for } k \text{ even.} \end{cases}$$

$$a_{t(k)} = \begin{cases} -\dfrac{2nV_{\rm out}}{k\pi}, & \text{for } k \text{ odd} \\ 0, & \text{for } k \text{ even.} \end{cases} \quad (6)$$

As the system in Fig. 5 is an linear, time-invariant (LTI) system, the steady-state current can be calculated by

$$\begin{aligned} i_t &= \frac{v_z - v_{s4} - v_t}{Z_0} \\ &= \sum_{k=1}^{\infty} |G(jk\omega_{\rm sw})| \{ a_{z(k)} \cos(k\omega_{\rm sw} t + \angle G(jk\omega_{\rm sw})) \\ &\quad - a_{s4(k)} \cos(k\omega_{\rm sw} t - k\varphi_{s4} + \angle G(jk\omega_{\rm sw})) \\ &\quad - a_{t(k)} \cos(k\omega_{\rm sw} t - k\varphi_{t1} + \angle G(jk\omega_{\rm sw})) \\ &\quad + a_{t(k)} \cos(k\omega_{\rm sw} t - k\varphi_{t2} + \angle G(jk\omega_{\rm sw}))\} \end{aligned} \quad (7)$$

where $G(jk\omega_{\rm sw})$ is the transfer function from v_{lr} to i_t, i.e., the impedance at the frequency $\frac{k\omega_{\rm sw}}{2\pi}$.

The transferred steady-state power is

$$\begin{aligned} p &= v_t i_t \\ &= nV_{\rm out} \sum_{k=1}^{\infty} \left\{ \frac{|G(jk\omega_{\rm sw})|}{k\pi} 2\sin\left(\frac{k\varphi_{t1} - k\varphi_{t2}}{2}\right) \right. \\ &\quad \times \left[a_{z(k)} \sin\left(\frac{k\varphi_{t1} + k\varphi_{t2}}{2} + \angle G(jk\omega_{\rm sw})\right) \right. \\ &\quad - a_{s4(k)} \sin\left(\frac{k\varphi_{t1} + k\varphi_{t2}}{2} - k\varphi_{s4} + \angle G(jk\omega_{\rm sw})\right) \\ &\quad - a_{t(k)} \sin\left(\frac{k\varphi_{t1} + k\varphi_{t2}}{2} - k\varphi_{t1} + \angle G(jk\omega_{\rm sw})\right) \\ &\quad \left. \left. + a_{t(k)} \sin\left(\frac{k\varphi_{t1} + k\varphi_{t2}}{2} - k\varphi_{t2} + \angle G(jk\omega_{\rm sw})\right)\right] \right\}. \end{aligned} \quad (8)$$

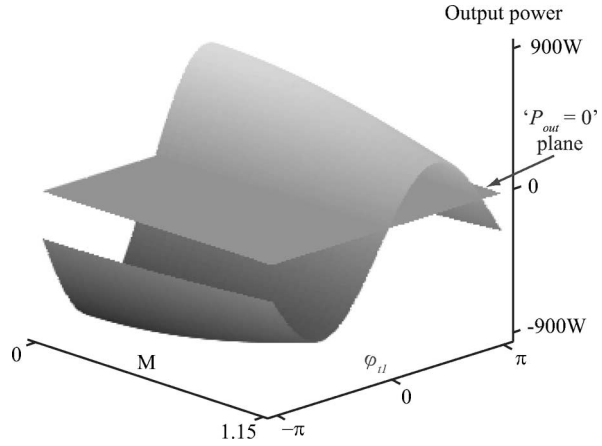

Fig. 7. Dependency of power on φ_{t1} and M for $n = 14$, $V_{\rm in} = 400$ V, $t = 0$, and $\varphi_{s4} = \pi$.

When the turns ratio n of the transformer is increased, the power that can be transferred through the converter increases, but if n is increased above a certain value, the reactive power increases as well. This reactive power results in higher device stresses and higher losses since the phase shift angle has to be increased. Therefore, the turns ratio for the prototype presented in Section II-E is selected to be 14 in order to get a high efficiency and to be able to transfer the required power for every possible converter state.

As mentioned earlier, the phase shift angles φ_{s4}, φ_{t1}, and φ_{t2} can be selected independently. In the actual implementation, $\varphi_{s4} = \pi$ and $\varphi_{t2} = \varphi_{t1} + \pi$ are selected because this choice enables the maximum power transfer. Independent of the modulation factor, which is defined through the machine's operating point, it is possible to control the power through the variation of φ_{t1}, as shown in Fig. 7. The output power is also slightly dependent on the machine's electrical angle, but this influence is small and it can also be eliminated with the variation of φ_{t1}. It is worth noticing that for the given parameter values, the maximum power that can be transferred from $V_{\rm in}$ to $V_{\rm out}$ (positive power) is higher than the power that can be transferred from $V_{\rm out}$ to $V_{\rm in}$ (negative power). In a normal, ideal, dual active bridge converter, the positive and negative maximum powers are equal [14]. As the resistance in the conventional dual active bridge is quite small, reality matches the ideal operation quite well. For the motor used in this paper, the zero-sequence resistance is significantly higher because it was designed for lower power levels (see Fig. 11). Thus, the voltage drop across this resistance causes an unbalance between the positive and the negative transferable power. Depending on the choice of n, $V_{\rm in}$, and $V_{\rm out}$, the positive or negative power maximum is higher.

Fig. 8 shows the actual controller. Other control schemes that use the other DOFs (see Table I) will be described in future publications along with an analysis to select the best DOFs to use.

C. Simulation of MFCS-I

Simulations of the model in Fig. 3(b) are carried out with the Simplorer software using the controller from Fig. 8, the machine

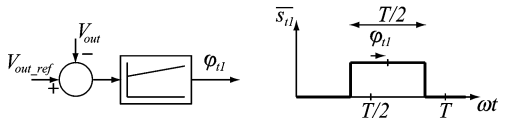

Fig. 8. Output voltage control of the MFCS-I.

TABLE I
DOFs

Controller degrees of freedom:
φ_{s4}: phase-shift angle of v_{s4}
φ_{t1}: phase-shift angle of v_{t1}
φ_{t2}: phase-shift angle of v_{t2}
Converter degrees of freedom:
n: turns ratio

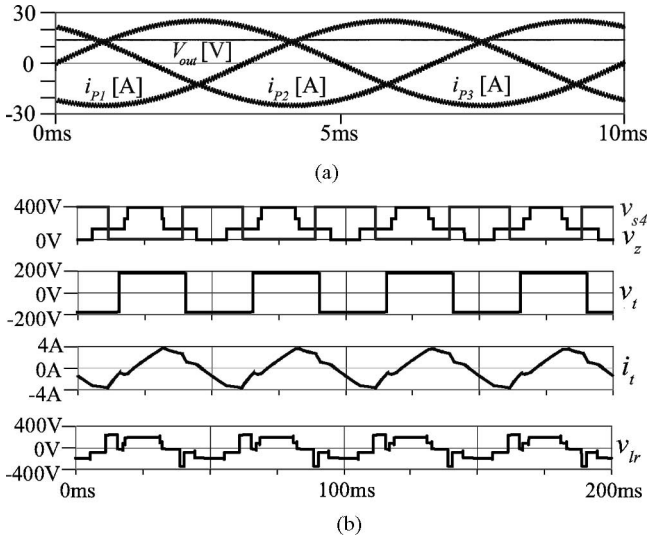

Fig. 9. Simulation results for MFCS-I with parameters given in Table II. (a) Phase currents and output voltage. (b) Zoom: Converter voltages (as introduced in Fig. 5).

TABLE II
PARAMETERS OF THE MFCS

Parameter	Value
motor parameters	see Tables IV and V
motor speed	1500 rpm
switching frequency f	20 kHz
input voltage V_{in}	400 V
output voltage V_{out}	14 V
motor power	3 kW
converter output power	300 W
turns ratio n	14

model from Fig. 14 (explained in Section II-D), and a resistive load. Fig. 9 shows the simulation results for the prototype machine described in Section II-E with the parameters given in Table II. It can be seen that the output voltage, and thus, the output power are constant over one motor period. Furthermore, the voltage-time product of the transformer is below the desired value, and saturation is avoided.

In Table III, the characteristic results of the simulation are listed. As the zero-sequence resistance of the investigated machine is quite large, an efficiency of only about 70% is reached. Since the machine is not intended for use in automotive applications, an asynchronous motor for a parallel hybrid car is also measured. The measurement shows that the impedance is significantly smaller. For a relevant machine like this, the efficiency of the dc-to-dc conversion is above 85%. The efficiency can be further increased by choosing a new control scheme and including the DOFs specified in Table I, as will be shown in future publications.

TABLE III
SIMULATION RESULTS OF MFCS I

Parameter	Value for MFCS-I	Value for the conventional inverter
I_{R01rms}	0.4 A	0.1 A
I_{R02rms}	0.8 A	0.3 A
I_{R03rms}	3.0 A	1.9 A
I_{R04rms}	14.0 A	9.2 A
I_{t1rms}	19.8 A	-
I_{s4rms}	1.8 A	-

D. Detailed Analysis of the Zero-Sequence Impedance

Today, a 2-D finite-element method (FEM) is typically used for analyzing the electromagnetic field and performance of electric machines. The high frequency of the zero-sequence voltage causes additional problems since the magnetic flux is reduced and the losses are increased due to eddy currents, and the skin and proximity effects must be taken into account in the windings and laminated iron core. The conductors of the windings can be discretized using a dense finite-element mesh. Due to the high-frequency eddy currents in the iron core, the magnetic field distribution is nonuniform over the thickness of the laminations, making the problem 3-D in addition to being time-dependent and nonlinear. In practice, it is impossible to model the eddy currents in each separate lamination, and homogenization techniques have been developed for the time-domain analysis of the problem [16]. In the linear case, the skin effect can be easily included in a frequency-domain analysis, provided that complex permeability can be used in the finite-element software (see [17] and [18]).

Fig. 10(a) illustrates the magnetic field strength and current density distributions over the thickness d of a single lamination. The winding currents flowing in the y-direction produce a magnetic field strength in the z-direction, and the sinusoidal variation of the magnetic field strength induces the eddy current density $J_y(x)$ in the y-direction. The higher the frequency is, the more the magnetic field strength $H_z(x)$ is reduced in the middle of the lamination due to eddy currents, as shown in Fig. 10(b). The magnetic field strength is given by

$$\underline{H}_z(x) = \underline{H}_0 \frac{\cosh\left(\frac{1+j}{\delta}x\right)}{\cosh\left(\frac{1+j}{\delta}\frac{d}{2}\right)} \tag{9}$$

where $\underline{H}_0$ is the field strength at the surface of the lamination and $\delta = \frac{1}{\sqrt{2\pi f \sigma \mu}}$ is the skin depth, f being the frequency, σ the conductivity, and μ the permeability. In order to include this effect in the FEM simulation, the laminations are replaced by a

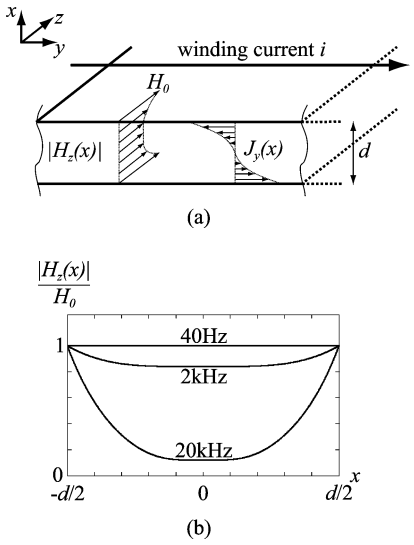

Fig. 10. Core lamination model and magnetic field, and magnetic field distribution in the lamination. (a) Modelling of the machine's lamination by a y–z-direction infinite sheet. (b) Magnetic field in the lamination.

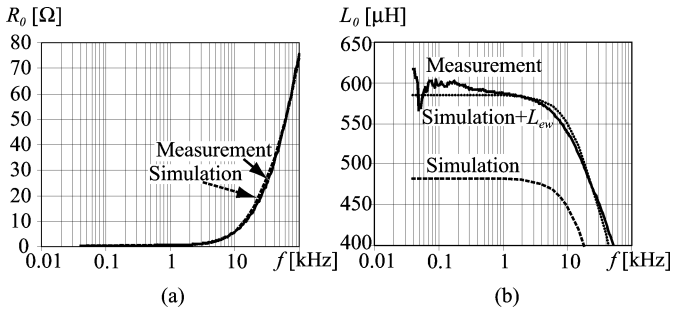

Fig. 11. Measured and simulated zero-sequence impedance of the synchronous motor. Lamination parameters for the simulation: thickness $d = 0.5$ mm, initial permeability $\mu_0 = 100$, conductivity $\sigma = 4$ MS/m. (a) Zero-sequence resistance. (b) Zero-sequence inductance.

nonconductive material with complex permeability [19]

$$\underline{\mu}_e = \mu \frac{\tanh\left(\dfrac{1+j}{\delta}\dfrac{d}{2}\right)}{\dfrac{1+j}{\delta}\dfrac{d}{2}}. \tag{10}$$

The zero-sequence impedance is analyzed using the 2-D FEM analysis of the COMSOL software. Fig. 11 shows the results of the measurements (solid) and FEM simulations. The deviations of the simulated resistance from the measured one are below 12% in Fig. 11(a). Reasons for this difference are that the geometrical details of the machine are not known exactly and that neither the end windings nor the cabling are taken into account. The deviation of simulated inductance from the measured one in Fig. 11(b) is due to the same reason. As the end winding inductance is not negligible, it should be considered. The end winding leakage inductance can be approximately calculated, as in [20], by

$$L_{\mathrm{ew}} = 2n^2 p l_{\mathrm{ew}} \mu_0 \lambda_{\mathrm{ew}} \tag{11}$$

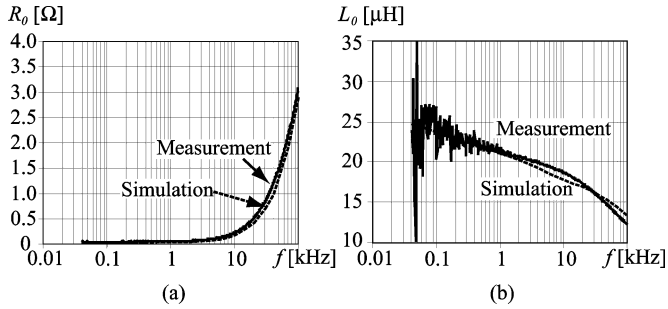

Fig. 12. Measured and simulated zero-sequence impedance for a 15 kW motor. Lamination parameters for the simulation: thickness $d = 0.2$ mm, initial permeability $\mu_0 = 250$, conductivity $\sigma = 2.8$ MS/m. (a) Zero-sequence resistance. (b) Zero-sequence inductance.

where n is the number of winding turns in series per strand, p the number of pole pairs, l_{ew} the average length of the coil ends, and λ_{ew} the end winding leakage factor. For the actual motor with $n = 30$, $p = 4$, $l_{\mathrm{ew}} \approx 9.5$ cm, and $\lambda_{\mathrm{ew}} \approx 0.35$, it follows for the zero-sequence inductance $L_{\mathrm{ew}0} = \frac{L_{\mathrm{ew}}}{3} \approx 10\ \mu$H. After adding this end winding leakage inductance, it is obvious that the simulation for the inductance also matches rather well, which is shown by a dotted line in Fig. 11(b).

Electrical machines used in hybrid cars usually have higher power ratings than the prototype machine. The relative resistance (i.e., the per-unit resistance) decreases with machine size, and so do the relative resistive losses as well as the relative iron losses. Therefore, the zero-sequence resistance for machines intended for hybrid vehicles is smaller than that of the prototype machine even for high frequencies, which means that the losses decrease and the efficiency increases significantly for the real application. These considerations are confirmed by the measurement (solid) and simulation of the zero-sequence impedance of a 15 kW machine for automotive applications, as shown in Fig. 12. Since the machine has only one pole pair, and as it is rather short compared to the diameter, the end winding has a larger influence and an estimate of the end winding impedance is included in the simulation. The deviations in Fig. 12(a) of the simulated resistance from the measured one are below 17%. Again, reasons for this difference are that the geometrical details of the machine are not known exactly and that the cabling is not taken into account. The deviation of simulated inductance from the measured one has the same reason, as in Fig. 12(b).

To find an adequate simulation model for the machine's impedance, the magnetic flux has to be investigated. The three voltages v_{P1}, v_{P2}, and v_{P3} excite a magnetic flux in the machine. One part of this flux, called the main flux Ψ_m, is linked with all three phases. The other part of the flux, consisting of the slot leakage flux, the end winding leakage flux, etc., is represented by the leakage flux Ψ_σ.

Fig. 13(a) shows a COMSOL simulation for symmetrical, sinusoidal three-phase currents, and Fig. 13(b) for zero-sequence currents. Suppose there is no saturation, then the main flux of the individual winding phases sum up to zero due to the spatial distribution if a zero-sequence current flows through the machine. Therefore, a zero-sequence current excites only a leakage flux.

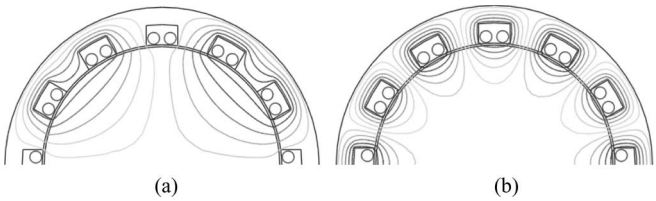

Fig. 13. COMSOL simulation of the magnetic flux for (a) symmetrical, sinusoidal currents and (b) zero sequence current.

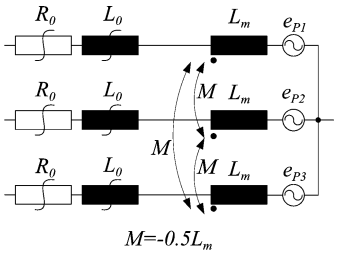

Fig. 14. Simplified equivalent circuit of the motor.

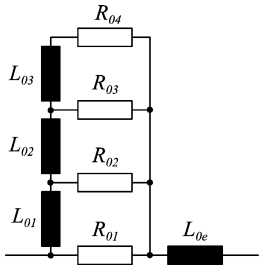

Fig. 15. Equivalent circuit representing the frequency-dependent R_0 and L_0 in Fig. 5.

Although the local flux is influenced by the zero-sequence current, the total torque is not. Due to the spatial distribution of the zero-sequence current, the forces cancel to zero, and consequently, the total torque of a machine with zero-sequence current is equal to the one of a machine without zero-sequence current.

To model these effects, the equivalent motor circuit depicted in Fig. 14 is used. As the losses due to skin and proximity effects and the core losses are frequency dependent, the resistance R_0 changes with the frequency. The same applies to the inductance L_0. Fig. 15 shows the four-step R–L ladder circuit for modeling the frequency dependence of the zero-sequence impedance. The parameters presented in Table IV were calculated to fit the measured impedance of the machine shown in Fig. 11. The mutual inductances also depend on the frequency, but as only the zero-sequence current is relevant for the dc–dc converter, this effect is omitted in the equivalent circuit.

E. Design and Experimental Results of MFCS-I

To verify the functionality of the proposed MFCS-I, a synchronous motor with accessible star point (and integrated secondary windings in order to also allow the evaluation of MFCS-II) with the parameters given in Table V has been designed. Fig. 16 shows the motor with the extra windings as described in Section II-F.

TABLE IV
PARAMETERS FOR THE EQUIVALENT CIRCUIT IN FIG. 15

Parameter	Value
L_{0e}	1.01 mH
R_{01}	150.29 Ω
L_{01}	0.60 mH
R_{02}	32.25 Ω
L_{02}	0.21 mH
R_{03}	6.92 Ω
L_{04}	0.07 mH
R_{04}	1.49 Ω

TABLE V
PARAMETERS OF THE PROTOTYPE

Parameter	Value
number of poles	8
nominal speed	1500 rpm
input voltage V_{in}	250 V...400 V
motor power	3 kW
back EMFs e_R, e_S and e_T	67.8 Vrms at 1000 rpm

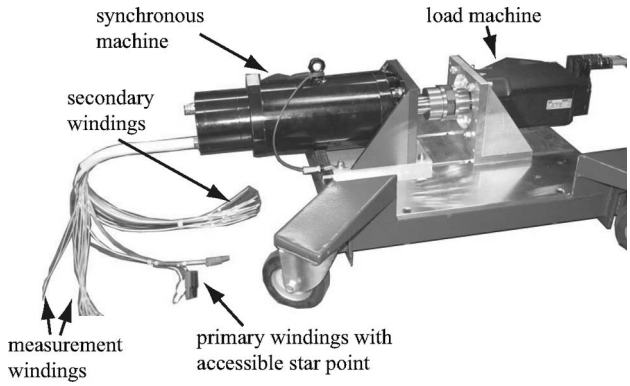

Fig. 16. Three-kilowatt permanent magnet synchronous motor with accessible star point (and secondary windings for MFCS-II).

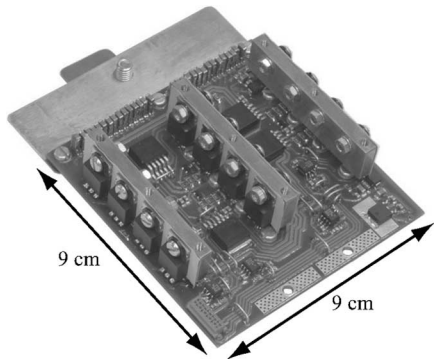

Fig. 17. Active secondary-side rectifier.

The motor is driven by a 6.8-kW three-phase back-to-back converter. The converter's inverter stage, fed from an external dc-link voltage, is used to drive the motor. The converter's rectifier stage is unused apart from one leg, which serves as the fourth leg in Fig. 3(b).

In the test system, the active output rectifier shown in Fig. 17 is used. The target system is assumed to include a 50 kW machine,

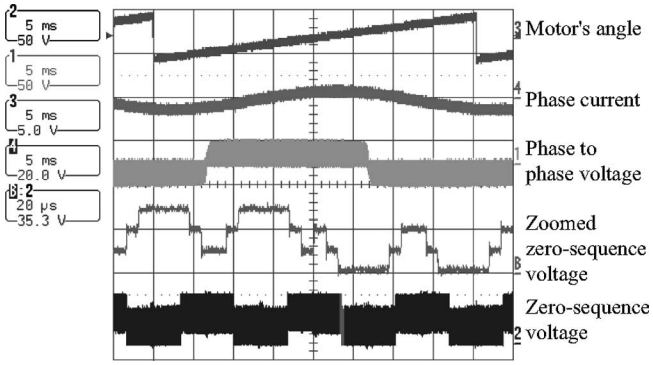

Fig. 18. Measurement of the zero-sequence voltage for a modulation index of $M = 0.5$ and an input voltage $V_{\rm in} = 50$ V.

the dc–dc converter having a nominal power of 1.5 kW and a maximum power of 5 kW. This leads from the 3-kW prototype machine to a dc–dc converter with a nominal power of 90 W and a maximum power of 300 W.

The results of the zero-sequence voltage measurement in Fig. 18 and the simulation in Fig. 4(b) match very well. The measurement of the zero-sequence impedance in Fig. 11 shows the high zero-sequence resistance, but as already stated, this problem will not occur in hybrid cars since electrical machines with low resistance are used (see Fig. 12).

Finally, the measurements in Fig. 19 show the results for the operation of the MFCS-I. The machine rotates at 370 r/min with an input voltage of 150 V, transferring 90 W via the dc–dc converter. It is obvious that it is possible to transfer power. Furthermore, the measurements agree very well with the simulations shown on the right, which were performed with the model presented in Section II-C.

F. Efficiency

In order to compare the presented MFCS-I to conventional converters, the efficiency has been measured for the prototype system. Then, analytical expressions are formed and scaled to higher power ratings in order to evaluate the efficiency at the power ratings typically used in hybrid cars.

To find the analytical expressions, the prototype motor's impedance is measured (cf. Section II-D) as well as the transformer's impedance, and their frequency-dependent analytical models are formed. The conduction parameters for the switches are taken from the datasheets. With these impedances, analytical expressions for the different currents and their rms values, respectively, have been determined and are similar to (7). In addition, the switching losses have been measured and put in an analytic function, thus allowing calculation of the total losses. The equations have been validated with the prototype and they correspond very well with the measurements. For the setup described in Fig. 19, an efficiency of 60% was measured. As shown in Table VI, the main losses occur in the motor. This is caused by the relatively large zero-sequence resistance of the motor at the switching frequency, as described in Section II-D.

Since the zero-sequence resistance of machines used in hybrid cars is usually smaller (see Section II-D) and since the

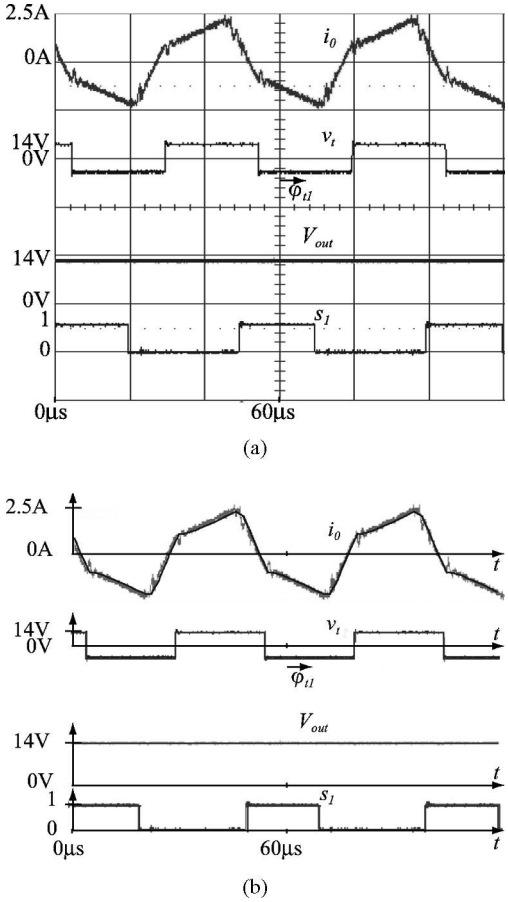

Fig. 19. Measurement and simulation results obtained with the test system. The input voltage $V_{\rm in} = 150$ V, output voltage $V_{\rm out} = 14$ V, transferred power $p_{\rm dc-dc} = 90$ W, rotational speed $n = 370$ rpm. (a) Measurement. (b) Simulation (dashed) and measurement.

TABLE VI
LOSSES FOR THE PROTOTYPE SYSTEM WITH THE INPUT VOLTAGE $V_{\rm in} = 150$ V, OUTPUT VOLTAGE $V_{\rm out} = 14$ V, TRANSFERRED POWER $p_{\rm dc-dc} = 90$ W, ROTATIONAL SPEED $n = 370$ R/MIN

Parameter	Calculated [W]	Measured [W]
Switching losses IGBTs	7.0	7.1
Conduction losses IGBTs	0.2	0.2
Sw. losses MOSFETs	0.8	0.8
Cond. losses MOSFETs	0.1	0.1
Motor losses	51.7	52.4
Transformer losses	0.6	0.6

The losses correspond only to the additional losses introduced by the dc–dc converter.

calculations and the measurements do agree very well, the efficiency calculations have been scaled. The target system drives a 50 kW machine from a 200–500 V bus and the dc–dc converter transfers nominal 1.5 kW (maximal 5 kW) to the 14 V bus. The target motor's parameters were retrieved from the measurements presented in Section II-D. Appropriate switches, i.e., 200 A/1200 V insulated-gate bipolar transistors for the high-voltage side and eight parallel 75 A/40 V MOSFETs for the low-voltage side, and transformers were chosen and their switching and conduction parameters determined from measurements and/or their datasheets. The calculation typically yields efficiencies above 85% for a typical hybrid car converter system.

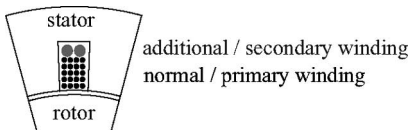

Fig. 20. Transformer integrated into the motor.

III. MFCS-II

In a second integration step, the galvanic isolation of $V_{\rm out}$ can also be integrated into the motor [see Fig. 3(c)] in order to reduce the costs and weight further. To do so, additional windings must be placed in the slots together with the conventional windings.

Fig. 20 shows a simplified sketch of the integration of the transformer proposed for the MFCS-II. The conventional motor windings act as the primary windings of the three transformers, and the additional windings form the secondary windings. The stator iron core of the electric machine is used as the magnetic core of the transformer. Further elaborations on the MFCS-II are provided in [11] and [21].

As the transformer is integrated into the machine, only one auxiliary bridge leg and a secondary rectifier are required to realize an isolated dc–dc converter. In order to prove the functionality of the MFCS-II, simulations similar to that presented in Section II-C for the MFCS-I have been performed. The motor/transformer parameters have been measured and implemented in the simulation. In a next step, the hardware for the MFCS-II is taken into operation and the simulations are verified.

IV. Conclusion

By integrating the dc–dc converter, which connects the low- and high-voltage buses of a hybrid vehicle, into the traction inverter and electrical machine, the total system costs and weight can be reduced. In this paper, a new concept for integrating the converter is presented and verified by simulations and measurements. With the first concept MFCS-I, the inverter and the machine are used to implement a primary bridge leg of an isolated full-bridge dc–dc converter. In addition to the MFCS-I, the MFCS-II is briefly described in this paper. The second concept offers an even higher degree of integration, since it allows one not only to replace one leg of the dc–dc converter by the inverter stage, but also to fully integrate the transformer in the machine.

In order to validate the MFCS-I concept, a scaled prototype with a 3-kW prototype machine and a 90-W dc–dc converter has been constructed. The resulting measurements agree very well with the simulations and the analytical models. Furthermore, the zero-sequence resistance of the machine, which has significant influence on the system performance, has been analyzed by FEM simulations, and agrees very well with the measurement values. Efficiencies of 60–70% were measured for phase shift operation, but the efficiency might be increased with an optimized switching scheme. Therefore, in a next step, different control schemes with the DOFs described in Table I will be analyzed. Further, the saturation in the machine has to be examined.

Based on these analytical models, a target system with a 50 kW machine and a 1.5-kW dc–dc converter has been designed for the MFCS-I concept, where an efficiency greater than 85% is likely for the dc–dc converter with a conventional modulation scheme. In a case where an optimized switching scheme is applied, an efficiency above 91% could be reached.

References

[1] S. Williamson, M. Lukic, and A. Emadi, "Comprehensive drive train efficiency analysis of hybrid electric and fuel cell vehicles based on motor-controller efficiency modeling," *IEEE Trans. Power Electron.*, vol. 21, no. 3, pp. 730–740, May 2006.

[2] A. Emadi, S. Williamson, and A. Khaligh, "Power electronics intensive solutions for advanced electric, hybrid electric, and fuel cell vehicular power systems," *IEEE Trans. Power Electron.*, vol. 21, no. 3, pp. 567–577, May 2006.

[3] A. Emadi, M. Ehsani, and J. Miller, "Advanced silicon rich automotive electrical power systems," in *Proc. 18th Digit. Avionics Syst. Conf.*, St Louis, MO, Oct. 24–29, 1999, vol. 2, pp. 8.B.1-1–8.B.1-8.

[4] J. Wang, F. Peng, J. Anderson, A. Joseph, and R. Buffenbarger, "Low cost fuel cell converter system for residential power generation," *IEEE Trans. Power Electron.*, vol. 19, no. 5, pp. 1315–1322, Sep. 2004.

[5] K. Moriya, H. Nakai, Y. Inaguma, H. Ohtani, and S. Sasaki, "A novel multi-functional converter system equipped with input voltage regulation and current ripple suppression," in *Conf. Rec. 2005 Ind. Appl. Conf. 40th IAS Annu. Meeting*, Oct. 2–6, vol. 3, pp. 1636–1642.

[6] S. J. Lee and S. K. Sul, "An integral battery charger for 4 wheel drive electric vehicle," in *Conf. Rec. 1994 IEEE Ind. Appl. Soc. Annu. Meeting*, Oct. 2–6, vol. 1, pp. 448–452.

[7] T. Franke, "Switching device for linking various electrical voltage levels in a motor vehicle," Patent WO/2006/105 840, Oct. 2006.

[8] S. Kinoshita, K. Fujita, and J. Ito, "Electric system for electric vehicle," Patent 6 066 928, May 2000 [Online]. Available: http://www.freepatentsonline.com/6066928.html

[9] S. Sasaki, "Multiple power source system and apparatus, motor driving apparatus, and hybrid vehicle with multiple power source system mounted thereon," Patent 6 476 571, Nov. 2002 [Online]. Available: http://www.freepatentsonline.com/6476571.html

[10] H. Plesko, J. Biela, and J. W. Kolar, "Drehstromantriebssystem mit hochfrequent potentialgetrennter bidirektionalen Kopplung der Versorgungsspannungen," Patent 01 220/06, 2006.

[11] J. Biela, H. Plesko, and J. W. Kolar, "Drehstromantriebssystem mit motorintegriertem Hochfrequenztrafo zur bidirektionalen Kopplung der Versorgungsspannungen," Patent 01 219/06, 2006.

[12] J. M. Nagashima, D. S. Carlson, C. C. Stancu, S. Hit, and K. M. Rahman, "Auxiliary power conversion by phase-controlled rectification," Patent 6 617 820, Sep. 2003 [Online]. Available: http://www.freepatentsonline.com/6617820.html

[13] C. C. Stancu, S. Hiti, and J. Nagashima, "Auxiliary power conversion for an electric vehicle using high frequency injection into a PWM inverter," Patent 6 262 896, Jul. 2001 [Online]. Available: http://www.freepatentsonline.com/6262896.html

[14] M. Kheraluwala, R. Gasgoigne, D. Divan, and E. Bauman, "Performance characterization of a high power dual active bridge dc/dc converter," in *Conf. Rec. 1990 IEEE Ind. Appl. Soc. Annu. Meeting*. Seattle, WA, Oct. 7–12, vol. 2, pp. 1267–1273.

[15] H. Tao, A. Kotsopoulos, J. L. Duarte, and M. A. M. Hendrix, "Transformer–coupled multiport ZVS bidirectional dc–dc converter with wide input range," *IEEE Trans. Power Electron.*, vol. 23, no. 2, pp. 771–781, Mar. 2008.

[16] P. Dular, J. Gyselinck, and L. Krähenbühl, "A time-domain finite element homogenization technique for lamination stacks using skin effect subbasis functions," *COMPEL*, vol. 25, pp. 6–16, 2006.

[17] P. Dular, J. Gyselinck, C. Geuzaine, N. Sadowski, and J. Bastos, "A 3-d magnetic vector potential formulation taking eddy currents in lamination stacks into account," *IEEE Trans. Magn.*, vol. 39, no. 3, pp. 1424–1427, May 2003.

[18] L. Dalessandro, W. Odendaal, and J. Kolar, "HF characterization and nonlinear modeling of a gapped toroidal magnetic structure," *IEEE Trans. Power Electron.*, vol. 21, no. 5, pp. 1167–1175, Sep. 2006.

[19] G. Grandi, M. Kazimierczuk, A. Massarini, U. Reggiani, and G. Sancineto, "Model of laminated iron-core inductors for high frequencies," *IEEE Trans. Magn.*, vol. 40, no. 4, pp. 1839–1845, Jul. 2004.

[20] R. Richter, *Elektrische Maschinen*. Cambridge, MA: Birkhäuser, 1963.
[21] H. Plesko, J. Biela, J. Luomi, and J. W. Kolar, "Novel concepts for integrating the electric drive and auxiliary dc–dc converter for hybrid vehicles," in *Proc. 20nd Annu. IEEE Appl. Power Electron. Conf. (APEC) 2007*, Anaheim, CA, Feb. 25–Mar. 1, pp. 1025–1031.

Hanna Plesko (S'06) studied information technology and electrical engineering at the Swiss Federal Institute of Technology (ETH) Zurich, Zurich, Switzerland, and the M.Sc. degree in electric power systems and control engineering. Since November 2005, she is working toward the Ph.D. degree at the Power Electronic Systems Laboratory, ETH Zurich.

Her past research interests include designing and realizing communication electronics for a medical blood pump system. Her current research interests include multifunctional converter systems for automotive applications.

Jürgen Biela (S'04) studied electrical engineering at Friedrich Alexander University of Erlangen (FAU Erlangen), Nuremberg, Germany, and received the Diploma degree (with honours) in October 2000. He received the Ph.D. degree in December 2005 from the Power Electronics Systems Laboratory (PES), Swiss Federal Institute of Technology (ETH) Zurich, Zurich, Switzerland.

He is currently working as a PostDoc at ETH. During his studies, he dealt, in particular, with resonant dc-link inverters at Strathclyde University, Scotland, and the active control of series-connected integrated gate commutated thyristors (IGCTs) at the Technical University of Munich, Germany. He was engaged in research on inverters with very high switching frequencies, SiC components, and electromagnetic compatibility at the Research Department of A&D Siemens, Germany. His current research interests include design, modeling, and optimization of power factor-correction (PFC)/dc–dc converters with emphasis on passive components and the design of pulse power systems.

Jorma Luomi (M'92) received the M.Sc.(Eng.) and D.Sc.(Tech.) degrees from Helsinki University of Technology, Espoo, Finland, in 1977 and 1984, respectively.

He joined Helsinki University of Technology in 1980, and from 1991 to 1998, he was a Professor at Chalmers University of Technology. He is currently a Professor in the Department of Electrical Engineering, Helsinki University of Technology. His current research interests include the areas of electric drives, electric machines, and numerical analysis of electromagnetic fields.

Johann W. Kolar (S'89–M'91–SM'04) studied industrial electronics at the Vienna University of Technology, Vienna, Austria, from where he also received the Ph.D. degree (*summa cum laude*).

From 1984 to 2001, he was with the Vienna University of Technology, where he was teaching and conducting research in close collaboration with the industry. He is currently the Professor and Head of the Power Electronics Systems Laboratory, Swiss Federal Institute of Technology (ETH) Zurich, Zurich, Switzerland, since Feb. 1, 2001. He has proposed numerous novel converter topologies, e.g., the Vienna rectifier and the three-phase ac–ac sparse matrix converter concept. He is the author or coauthor of more than 200 scientific papers in international journals and conference proceedings. He is the holder of more than 50 patents. His current research interests include ultracompact intelligent ac–ac and dc–dc converter modules employing latest power semiconductor technology (SiC), novel concepts for cooling and active electromagnetic interference filtering, multidisciplinary simulation, bearing-less motors, power microelectromechanical systems, and wireless power transmission.